Plasmonically Enhanced Photocatalytic Hydrogen Production from Water: The Critical Role of Tunable Surface Plasmon Resonance from Gold−Silver Nanoshells

Chien-Hung Li,[†] Min-Chih Li,[‡,§] Si-Ping Liu,[‡,§] Andrew C. Jamison,[†] Dahye Lee,[⊥] T. Randall Lee,*[,†] and Tai-Chou Lee*[,‡]

[†]Department of Chemistry and the Texas Center for Superconductivity, University of Houston, 4800 Calhoun Road, Houston, Texas 77204-5003, United States

[⊥]Materials Science & Engineering, University of Houston, Houston, Texas 77204, United States

[‡]Department of Chemical and Materials Engineering, National Central University, 300 Jhongda Road, Jhongli City 32001, Taiwan

ⓈSupporting Information

ABSTRACT: Gold−silver nanoshells (GS-NSs) having a tunable surface plasmon resonance (SPR) were employed to facilitate charge separation of photoexcited carriers in the photocalytic production of hydrogen from water. Zinc indium sulfide ($ZnIn_2S_4$; ZIS), a visible-light-active photocatalyst, where the band gap varies with the [Zn]/[In] ratio, was used as a model ZIS system (E_g = 2.25 eV) to investigate the mechanisms of plasmonic enhancement associated with the nanoshells. Three types of GS-NS cores with intense absorptions centered roughly at 500, 700, and 900 nm were used as seeds for preparing GS-NS@ZIS core−shell structures via a microwave-assisted hydrothermal reaction, yielding core−shell particles with composite diameters of ∼200 nm. Notably, an interlayer of dielectric silica (SiO_2) between the GS-NSs and the ZIS photocatalyst provided another parameter to enhance the production of hydrogen and to distinguish the charge-transfer mechanisms. In particular, the direct transfer of hot electrons from the GS-NSs to the ZIS photocatalyst was blocked by this layer. Of the 10 particle samples examined in this study, the greatest hydrogen gas evolution rate was observed for GS-NSs having a SiO_2 interlayer thickness of ∼17 nm and an SPR absorption centered at ∼700 nm, yielding a rate 2.6 times higher than that of the ZIS without GS-NSs. The apparent quantum efficiencies for these core−shell particles were recorded and compared to the absorption spectra. Analyses of the charge-transfer mechanisms were evaluated and are discussed based on the experimental findings.

KEYWORDS: gold−silver nanoshells, surface plasmon resonance, photocatalyst, zinc indium sulfide, hydrogen energy
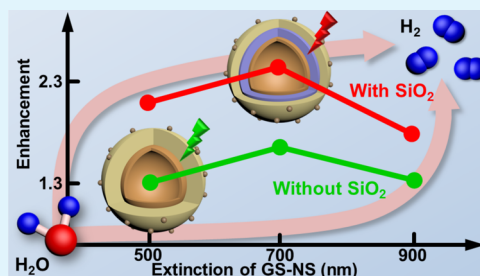
INTRODUCTION

Of all known renewable energy sources, solar energy stands as the most abundant and readily accessible. Consider, for example, that the amount of solar energy striking the earth every 40 min is approximately equal to the amount of energy consumed globally on an annual basis.[1] From this perspective, the United States is fortunate to have vast tracts of land that are suitable for constructing solar power plants; in fact, in the desert Southwest alone there are an estimated 250,000 square miles of suitable land receiving more than 4500 quadrillion British thermal units (Btu) of solar radiation per year.[1] Converting only 2.5% of that radiation into electricity would equal the total national energy consumption during all of 2006.

The abundance and availability of solar energy has sparked the exploration of a wide variety of solar conversion technologies, including those based on photovoltaic (direct solar to electric), photothermal (solar to heat), and photosynthesis (solar to fuel) conversion. In the latter technology, artificial photosynthesis mimics natural photosynthesis by converting water and/or carbon dioxide into fuels and oxygen using sunlight.[2] Splitting water to produce hydrogen and oxygen is one example, and it is the most promising replacement for fossil fuels without any pollutant.[3−7] The efficient utilization of solar energy is critical to the overall hydrogen production. In theory, the solar-to-hydrogen efficiency reaches 10% when the energy band gap is less than or equal to 2.4 eV.[5]

Unfortunately, almost all known photocatalyst materials suffer from fast recombination kinetics, which decreases the solar-to-hydrogen conversion.[8] Many approaches can be used to mitigate this problem. Incorporating metal nanoparticles into the photocatalyst matrixes has received much attention in recent years because of the unique surface plasmon resonance (SPR) properties associated with such nanostructures.[9−17] The intense SPR light absorption also generates a strong electric field close to the metal surface owing to the collective

oscillation of the conduction band electrons under irradiation. Mechanisms for the plasmonic enhancement of electron−hole formation in photocatalysts have been proposed[11,14] but are not yet fully understood. With spherical silver or gold nano-particles,[10−16] which exhibit SPR at wavelengths of ∼390−460 nm for silver and ∼520−640 nm for gold,[18,19] only limited additional light absorption relative to that existing for the photocatalyst occurs. Moreover, a UV-active TiO_2 photocatalyst usually serves as the model system to investigate charge-transfer mechanisms. Although SPR generated from simple metal nanoparticles can extend absorption of the composite system to the visible region, the overall activity under sunlight is still unsatisfactory.

In addition to their high electron−hole recombination rates under irradiation, most photocatalysts suffer a low solar-to-fuel conversion efficiency because of the limited range of wave-lengths at which they are active. To address these short-comings, we explore in this study a visible-light-active photocatalyst, $ZnIn_2S_4$ (ZIS),[20−23] that encapsulates unique metal−metal nanoshells[24,25] to investigate the effects of tuning (and broadening) the SPR absorption band on the efficiency of hydrogen production. In contrast to metal alloy nanoparticles, the absorption of light by our recently developed gold−silver nanoshells (herein denoted as GS-NSs) can be tuned to selected wavelengths by altering the size, shell thickness, and composition of the bimetallic shell, allowing unencumbered enhancements in the photocatalytic activity by tuning the extinctions to wavelengths beyond those at which ZIS absorbs.[20−25] Additionally, because of the presence of two metals with different intrinsic light-absorption properties, the extinction spectra of these GS-NSs exhibit a broad absorption of light that can range from the visible into the near-IR.[24] In this study, GS-NSs with three different absorption profiles were employed: namely, nanoshells with broad extinction spectra that peak at ∼500, 700, and 900 nm, as determined by the gold-to-silver ratio for the nanoshells and the degree to which the initial solid nanoparticle structure has been etched to form the nanoshell structure. For each of these GS-NSs, three different types were tested within the ZIS matrix: (1) the bare nanoshells without a silica (SiO_2) coating, (2) nanoshells with a thin (∼17 nm) SiO_2 coating, and (3) nanoshells with a thick (∼42 nm) SiO_2 coating. This unique set of nine photoactive combinations offers a systematic investigation of not only the role of the dielectric layer in mitigating electron−hole recombination within the photocatalyst matrix but also (and more importantly) the parameters that dictate the optimal coupling between the SPR of the nanoshells and the activity of the photocatalysts. The preparation of the "undoped" ZIS (i.e., ZIS without nanoshells) and composite core−shell particles was accomplished using a microwave-assisted hydrothermal synthesis. This low-temperature synthetic process is desirable because the structure and absorption of the GS-NSs remain intact. Further, all composite nanoshell−ZIS photocatalysts were prepared under the same experimental conditions to allow a meaningful comparison between samples based on hydrogen production from water, as contrasted with the undoped ZIS particles.

■ EXPERIMENTAL SECTION

Materials. Silver nitrate ($AgNO_3$; Aldrich), trisodium citrate dihydrate ($Na_3C_6H_5O_7 \cdot 2H_2O$; EM Science), potassium carbonate (K_2CO_3; Aldrich), hydrogen tetrachloroaurate(III) hydrate ($HAuCl_4 \cdot xH_2O$; Strem), nitric acid (HNO_3; EM Science), hydrochloric acid

(HCl; EM Science), ammonium hydroxide (NH_4OH; EM Science), tetraethylorthosilicate (TEOS; Aldrich), indium(III) nitrate hydrate [$In(NO_3)_3 \cdot xH_2O$; Alfa Aesar], zinc nitrate hexahydrate [$Zn(NO_3)_2 \cdot 6H_2O$; J.T. Baker], thioacetamide (TAA; C_2H_5NS; Sigma-Aldrich), dihydrogen hexachloroplatinate(IV) hexahydrate ($H_2PtCl_6 \cdot 6H_2O$; Alfa Aesar), potassium sulfite (K_2SO_3; Sigma-Aldrich), and sodium sulfide hydrate ($Na_2S \cdot xH_2O$; Sigma-Aldrich) were purchased from the indicated suppliers and used without modification. Water was purified to a resistivity of 18 MΩ·cm (Academic Milli-Q Water System; Millipore Corp.) and filtered using a 0.22 μm filter. All glassware used in the experiments were cleaned in an aqua regia solution (3:1 HCl/ HNO_3) and dried in an oven prior to use.

Preparation of Silver Nanoparticle Cores. Silver nanoparticles were prepared by the method of Lee and Meisel,[26] which involves the reduction of $AgNO_3$ by sodium citrate. An aliquot of $AgNO_3$ (0.0167 g, 0.100 mmol) was dissolved in 100 mL of water. The solution was brought to reflux, and then 2 mL of a 1% trisodium citrate solution was added under vigorous stirring. The reflux was maintained for 25 min. The solution turned yellow green, indicating the presence of silver nanoparticles. The solution was allowed to cool to room temperature (rt) and then centrifuged at 6000 rpm for 15 min. The nanoparticles were then redispersed in 12.5 mL of water. This procedure generated silver nanoparticles, where the size could be adjusted from 40 to 100 nm, depending on the concentration of the reactants.

Preparation of Hollow Gold−Silver Nanoshells (GS-NSs). The synthesis procedures for the hollow GS-NSs followed those reported previously,[24] with the basic solution of gold salt (K-gold solution) prepared using the method reported by Oldenburg et al.[27] Following this method, 0.025 g of K_2CO_3 was added to 100 mL of purified water, which was then injected with 2 mL of a 1% $HAuCl_4 \cdot H_2O$ solution. The mixture, initially yellow in color, became colorless 30 min after the reaction was initiated. The flask was then covered with aluminum foil to shield it from light, and the solution was stored in a refrigerator overnight. Various amounts of gold solution were added to the silver nanoparticles, depending on the desired level of the displacement of silver by gold and the associated shift in the peak SPR light absorption. Typical procedures for the nanoshells prepared for this report are as follows: for an SPR band at 500 nm, 10 mL of silver nanoparticles was mixed with 15 mL of K-gold solution and stirred for 5 h; for an SPR band at 700 nm, 10 mL of silver nanoparticles was mixed with 90 mL of K-gold solution and stirred for 5 h; for an SPR band at 900 nm, 10 mL of silver nanoparticles was mixed with 180 mL of K-gold solution and stirred for 5 h. The SPR band of each solution was tracked by UV−vis spectroscopy. The nanoshells were isolated by centrifugation at 6000 rpm for 15 min, and the supernatant was then decanted. The GS-NSs were redispersed in water prior to characterization and coating with SiO_2.

Preparation of SiO_2-Coated Hollow GS-NSs. The SiO_2-coated hollow GS-NSs were generated using a modified Stöber method.[28] In this procedure, 10 mL of a nanoshell solution was diluted to 20 mL and then mixed with ammonium hydroxide (2 mL) and ethanol (45 mL). Under vigorous stirring, 25−100 μL of TEOS was added to the solution, depending on the desired thickness of the SiO_2 shells. The mixture was then further stirred overnight at rt to allow the hollow GS-NSs to be encapsulated fully by the SiO_2 shells. The resulting solution was centrifuged at 6000 rpm for 20 min and the supernatant decanted, and the nanoshells were redispersed in ethanol. This procedure was repeated four times. Finally, the isolated composite nanoparticles were redispersed into 10 mL of ethanol for characterization and application.

Preparation of GS-NS@SiO_2@ZIS Composite Structures. In preparing undoped ZIS particles, zinc nitrate hexahydrate (0.3 mmol), indium(III) nitrate hydrate (0.6 mmol), and thioacetamide (2.4 mmol) were dissolved in 15 mL of deionized (DI) water under vigorous stirring for 20 min. The solution was then poured into a 30 mL quartz vessel. The hydrothermal reaction took place in a microwave reactor (Monowave 300, Anton Paar) at 120 °C for 10 min. The precipitates were collected and centrifuged at 8000 rpm for 5 min. The resulting particles were rinsed thoroughly with DI water several times and then dried in an oven at 80 °C for 12 h. For the synthesis of GS-NS@SiO_2@ZIS particles, a 250 μL aliquot of a

nanoshell solution was first dried, and the particles were then redispersed in 15 mL of DI water using ultrasonic vibration. Zinc nitrate hexahydrate (0.3 mmol), indium(III) nitrate hydrate (0.6 mmol), and thioacetamide (2.4 mmol) were dissolved under vigorous stirring. The reaction was then carried out in a microwave oven at 120 °C for 10 min. The as-prepared GS-NS@SiO$_2$@ZIS particles were collected by centrifugation and washed with DI water several times. Finally, the composite particles were placed in an oven at 80 °C for 12 h to remove excess water.

Characterization of Nanoparticles and Nanoshells. The size and morphology of the silver nanoparticles, GS-NSs, and SiO$_2$-coated GS-NSs were evaluated using a LEO-1525 scanning electron microscope operating at an accelerating voltage of 15 kV. To obtain high-resolution scanning electron microscopy (SEM) images, all samples were deposited on silicon wafers. Similarly, the size and morphology of the nanoshells were evaluated by employing a JEM-2000 FX transmission electron microscope operating at an accelerating voltage of 200 kV. Energy-dispersive X-ray (EDX) elemental mapping data were collected using a JEOL 2100F instrument. All transmission electron microscopy (TEM) samples were deposited on 300-mesh holey carbon-coated copper grids and dried overnight before analysis. UV−vis spectra were obtained using a Cary 50 Scan UV−vis spectrometer from 200 to 1000 nm, with all nanoshell samples suspended in water for the measurements.

Characterization of GS-NS@SiO$_2$@ZIS Composite Particles. To identify the collected samples in shorthand fashion, the composite particles are denoted as GS-NS(n)@SiO$_2$(m)@ZIS, where n indicates the wavelength of the peak SPR absorption and m is the thickness of the SiO$_2$ interlayer. For example, GS-NS(500)@SiO$_2$(17)@ZIS is the core−shell structure of the GS-NSs with an SPR absorption maxima of 500 nm, an interlayer SiO$_2$ thickness of ∼17 nm, and an encapsulating coating of ZIS. Extinction spectra were obtained using a UV−vis spectrophotometer (Jasco V-670) over the wavelength range from 300 to 900 nm. Crystal structures were determined using an X-ray diffractometer (Bruker Kappa Apex II) with a Cu Kα light source coupled with a nickel filter. The scan rate was set at 3°/min in the range of 20−80°. A JEOL JEM-2100 transmission electron microscope was used to image the structures of the particles. The samples without any SiO$_2$ interlayer are denoted as GS-NS(n)@ZIS. Steady-state photoluminescence (PL) spectra were obtained using a PL spectrometer (PerkinElmer LS-55). The GS-NS@SiO$_2$@ZIS samples with various SiO$_2$ thicknesses were suspended in ethanol for data collection. The concentrations of the particles were adjusted to exhibit the same absorption at 350 nm, corresponding to the maximum absorption of ZIS. This process was used to calibrate the level of ZIS content in each batch of core−shell particles. For collection of the PL spectra, the excitation wavelength was set at 375 nm.

Photocatalytic Hydrogen Production Reaction and Quantum Efficiency Measurements. The photocatalytic reaction for hydrogen production was conducted in a 225 mL custom-built cylindrical glass cell with a quartz side window and an illumination area of 23 cm^2. The sacrificial agent needed to drive the reaction was prepared by adding potassium sulfite (55 mmol) and sodium sulfide (77 mmol) to DI water (220 mL). An aliquot of 0.06 g of unmodified ZIS or GS-NS@SiO$_2$@ZIS particles was dispersed in the sacrificial solution, and 1 wt % dihydrogen hexachloroplatinate(IV) hexahydrate (33.4 μL) was added. The system was first irradiated with high-intensity light (400 mW/cm^2) for 1 h at 25 °C to photodeposit platinum nanoparticles on top of the ZIS surfaces. Finally, the photocatalytic reactor was irradiated with a 300 W xenon lamp. The intensity was set at 100 mW/cm^2 and monitored by an optical meter (Newport 1918-R). The temperature was maintained at 25 °C during the reaction, and hydrogen gas was collected for at least 5 h using a water displacement method.[29] The evolved gas was analyzed using a Shimadzu GC-14 gas chromatograph. Apparent quantum yields were determined using a compact monochromator (Sciencetech 9030) for the wavelength-dependent photocatalytic activity. The intensity of the transmitted light from the 300 W xenon lamp was ∼1000 mW/cm^2, which was reduced to ∼25−50 mW/cm^2 once the monochromator was included in the setup.

■ RESULTS AND DISCUSSION

SiO$_2$-Coated GS-NSs. The starting silver nanoparticles were analyzed by SEM to determine if the size and morphology were suitable for preparation of the targeted GS-NSs (see Figure S1 in the Supporting Information). All of the GS-NSs used in this project were prepared from the same initial silver nanoparticle sample based on the knowledge gained from our prior work to obtain targeted nanoshell sizes/exctinctions using optimal synthetic methods.[24,30] Upon completion of the gold salt galvanic replacement reaction on the silver nanoparticles to form the three types of GS-NSs, the morphologies of each of the samples were determined from images collected using TEM. Parts a−c of Figure 1 show the bare GS-NSs prepared
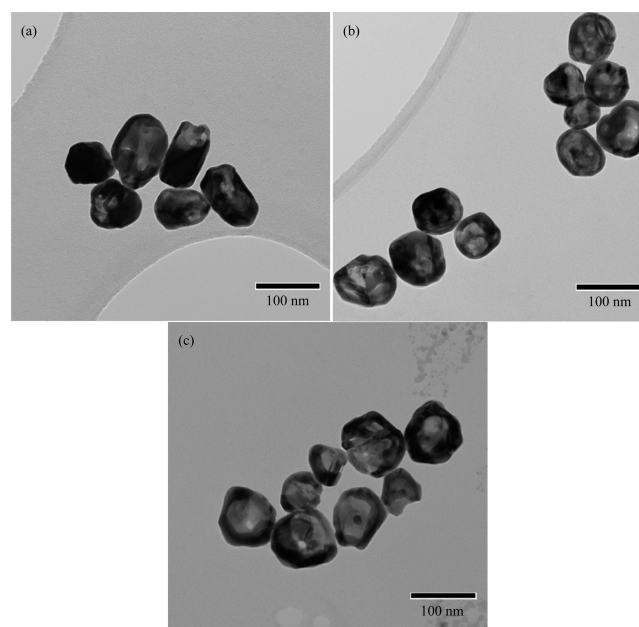

Figure 1. TEM images of hollow GS-NSs with peak intensities for the absorption bands at (a) ∼500, (b) ∼700, and (c) ∼900 nm.

from the three different levels of K-gold solution. As illustrated in these images, the average particle size for the bare GS-NSs was 80 ± 14 nm, and the associated particle size histograms are provided in Figure S2 in the Supporting Information. Due to the galvanic replacement reaction, where $3Ag + Au^{3+} \rightarrow 3Ag^+ + Au$, the shell of the resulting GS-NS becomes thinner with increasing exposure to K-gold solution.[24] This process gives rise to an increase in the gold content, in conjunction with a loss of silver and a reduction in the shell thickness, which leads to both a broadening of the SPR band of the extinction spectrum and a red shift in the absorption of light, as detailed below.[30] This shift in the relative content of the two metals is apparent in the EDX elemental mapping data and Ag/Au molar ratios for the GS-NS(500), GS-NS(700), and GS-NS(900) particles, which are provided in Figure S3 and Table S1 in the Supporting Information.

The three types of GS-NSs in Figure 1 were coated with two different thicknesses of the SiO$_2$ shell, and the data collected for these composite particles were compared with those of the GS-NSs prepared without SiO$_2$ shells. Our targeted shell thicknesses were 20 and 50 nm. The average thickness of the thinner SiO$_2$ coating was 17 ± 2 nm, as can be seen in the example TEM image in Figure 2a and the SEM images in Figure S4a,c,e in the Supporting Information. The average
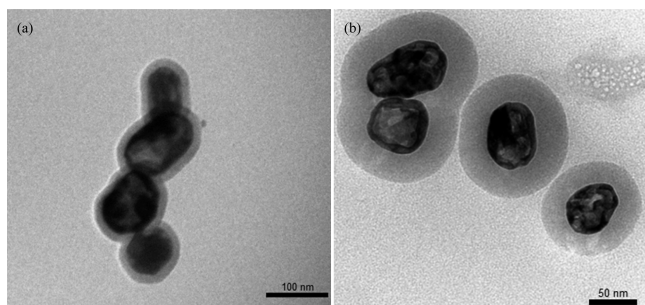
Figure 2. TEM images of the SiO$_2$-coated GS-NSs. The thicknesses of the SiO$_2$ coating are (a) ~17 and (b) ~42 nm.

GS-NS@ZIS particles in the Experimental Section). As shown in Figure 4a, the as-prepared ZIS particle aggregates consist of 1

Figure 4. (a) SEM image of an undoped ZIS particle and (b) TEM image of a GS-NS@SiO$_2$@ZIS composite aggregate prepared using the higher concentration of a ZIS precursor solution.

thickness of the thicker SiO$_2$ coating was 42 ± 8 nm, as shown in the TEM image in Figure 2b and the SEM images in Figure S4b,d,f in the Supporting Information. Figure 3a shows the extinction spectra for the hollow GS-NSs having three different absorption wavelengths (~500, 700, and 900 nm). The SPR band position of the nanoshells depends on the nanoparticle dimensions and, in particular, the shell thickness.[31] For our particles, the synthesis of each type of nanoshell started from the same volume of the silver nanoparticle solution, followed by the addition of different amounts of K-gold solution. As the volume of added K-gold solution increased, the extinction peak shifted to longer wavelengths, reflecting both a change in the core–shell structure and an increase in the presence of gold in the GS-NS.

Figure 3b shows the extinction spectra for the three samples of GS-NSs that were prepared with a peak position for the SPR band at ~700 nm: the uncoated nanoshell designated as GS-NS(700), the nanoshell with a thin layer of SiO$_2$ designated as GS-NS(700)@SiO$_2$(17), and the nanoshell with a thick layer of SiO$_2$ designated as GS-NS(700)@SiO$_2$(42). The red shift in the peak position of the SPR bands for the SiO$_2$-coated nanoshells, compared to the bare GS-NSs, can be attributed to the higher refractive index of SiO$_2$ (1.46)[32] compared to that of water (1.33).[33] Similarly, when the spectra of the two SiO$_2$-coated GS-NSs are compared, the peak position of the SPR band shows a slight red shift (744–747 nm) with increasing thickness of the SiO$_2$ layer. The optical properties of the SiO$_2$-coated GS-NSs appear to demonstrate that the thickness of the dielectric layer between the photocatalyst and GS-NS has only a minimal effect on the absorption wavelength of the GS-NSs.

Core–Shell Structures of Photocatalysts. The undoped ZIS particles were synthesized using a higher precursor concentration (5-fold of the concentration described for the
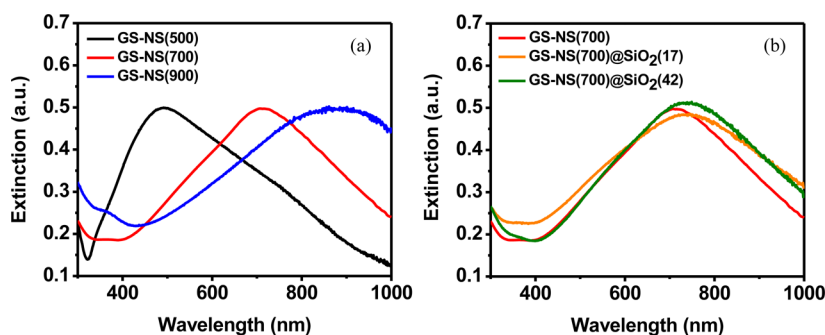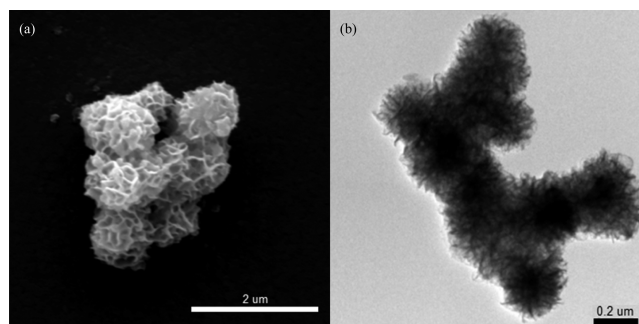
μm spheres with nanosheet structures covering the surfaces. When the GS-NS@SiO$_2$ nanoshells were added as seeds under these conditions, the resulting products were also particulate aggregates with somewhat smaller diameters (300−400 nm). From the contrast in the TEM image in Figure 4b, it appears that each aggregate contains more than one nanoshell. Thus, we determined that it was essential to understand better the reaction mechanism to further refine the reaction conditions.

Figure 5 shows the morphological changes of the GS-NS@SiO$_2$@ZIS particles at different reaction times through a series
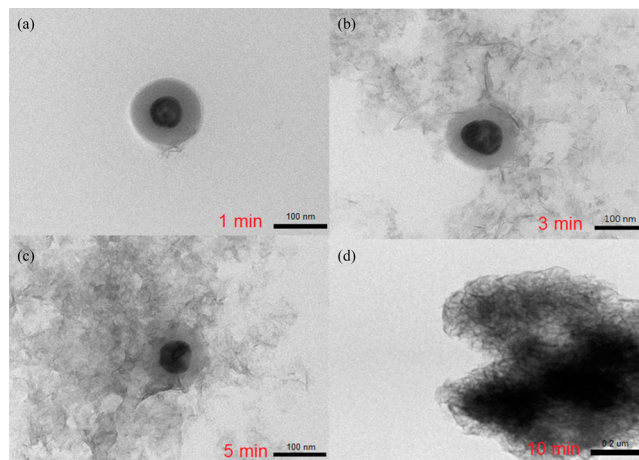

Figure 5. Series of TEM images illustrating the growth process of ZIS on the GS-NS@SiO$_2$ core at (a) 1, (b) 3, (c) 5, and (d) 10 min.

Figure 3. (a) UV−vis spectra of the nanoshells prepared without a SiO$_2$ coating: GS-NS(500), GS-NS(700), and GS-NS(900). (b) UV−vis spectra of GS-NS(700), GS-NS(700)@SiO$_2$(17), and GS-NS(700)@SiO$_2$(42).

of TEM images taken during the reaction. Figure 5a shows ZIS nucleation just after the start of the microwave-assisted hydrothermal process. The nanosheet structures began to grow within a few minutes (Figures 5b,c), while aggregates were generated toward the end of the reaction (Figure 5d). On the basis of these results, the precursor concentration was lowered during subsequent syntheses. The morphology of the resulting core−shell particles is shown in Figure 6a. After the
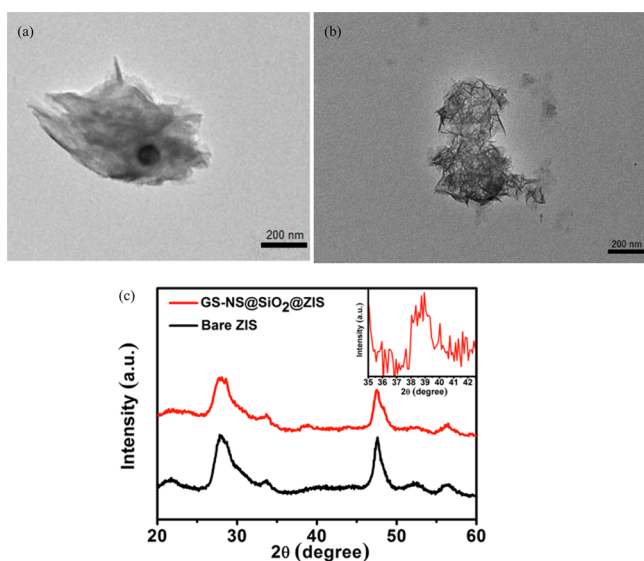

Figure 6. (a) TEM image of a GS-NS@SiO$_2$@ZIS core−shell particle prepared using a lower ZIS precursor concentration. (b) TEM image of an undoped ZIS particle prepared using a lower ZIS precursor concentration. (c) XRD patterns for the undoped ZIS and GS-NS(500)@SiO$_2$(17)@ZIS particles. The inset shows the enlarged diffraction pattern of the GS-NS(500)@SiO$_2$(17)@ZIS particle in the 2θ range between 35 and 42°, indicating the presence of the gold nanoshells.

adjustment, the TEM data show that the probability of finding composite particles that contain only one GS-NS is much higher. Therefore, we used this reduced precursor concentration exclusively for the balance of this study. For comparison, a TEM image of the undoped ZIS particles prepared from the lower ZIS precursor concentration is also shown in Figure 6b. The ZIS samples exhibit particlelike morphology with a lesser degree of aggregation and a particle size of around 200 nm. In addition, the ZIS coating on the GS-NS cores was dissolved using aqua regia to confirm that the SiO$_2$ interlayer is still present after the hydrothermal process. As illustrated in Figure S5 in the Supporting Information, it is evident that the SiO$_2$ coating remained intact.

We also investigated the crystal structures of the undoped ZIS and GS-NS@ZIS core−shell composite particles. For this purpose, we focused on the GS-NS(500)@SiO$_2$(17)@ZIS particles. Figure 6c shows the X-ray diffraction patterns of the two samples. The 2θ values at 27.8, 33.7, and 48.4° correspond to the cubic phase of ZIS. For GS-NS-containing particles, a weak diffraction peak at 2θ = 38−39° appeared, belonging to the (111) crystallographic plane of the bimetallic GS-NSs (see the enlarged XRD pattern in the inset of Figure 6c).[24] This result is consistent with the presence of hollow GS-NSs.

Parts a−d of Figure 7 plot the extinction spectra of four different samples: undoped ZIS particles and ZIS particles comprising GS-NSs with SPR absorption at ∼500, 700, and 900 nm. The thickness of the SiO$_2$ interlayer for the displayed data is ∼17 nm. The apparent quantum yield as a function of the wavelength was also plotted for each of the samples in the same figure, which will be discussed in detail in the following paragraph and examined further in the next section. As seen in Figure 7a, the absorption edge of the undoped ZIS can be extrapolated from the trajectory of the descending curve and is located at ∼550 nm, which corresponds to a band gap of ∼2.25 eV (E_g = 1240/λ).[22] Further, the shoulder at ∼375 nm observed in Figure 7b−d is plausibly associated with the
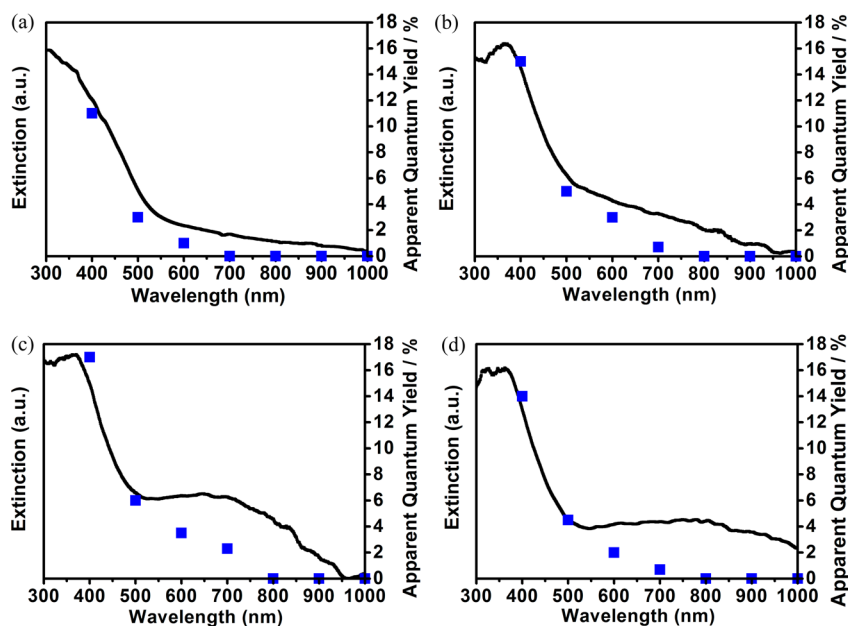

Figure 7. UV−vis spectra and apparent quantum yield data for (a) undoped ZIS particles along with that for (b) GS-NS(500)@SiO$_2$(17)@ZIS, (c) GS-NS(700)@SiO$_2$(17)@ZIS, and (d) GS-NS(900)@SiO$_2$(17)@ZIS composite particles. Quantum yield data points indicated by ■ were obtained with a monochromator, revealing wavelength-dependent photocatalytic activity.
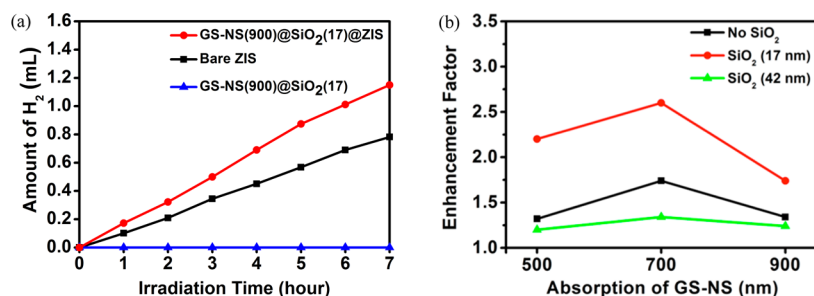
Figure 8. (a) Hydrogen evolution upon exposure to the light of a xenon lamp as a function of the reaction time for the undoped ZIS (squares), GS-NS(900)@SiO$_2$(17)@ZIS (circles), and GS-NS(900)@SiO$_2$(17) (triangles) particles. (b) Enhancement factors for the samples with different absorption properties and SiO$_2$ interlayers (■, no SiO$_2$; ●, ~17 nm; ▲, ~42 nm).

interband transitions of GS-NSs, which is consistent with modeling of these particles using Mie theory.[34] Additionally, for the GS-NS-containing ZIS samples (Figure 7b−d), a broader resonance at longer wavelength appears on each of the extinction spectra. The wavelength of this resonance correlates to that of the SPR from the designed GS-NSs. Accordingly, we conclude from the collective morphological, crystallographical, and optical analyses that the core−shell structure of the GS-NS@SiO$_2$@ZIS particles remains intact after microwave-assisted hydrothermal synthesis.

Photocatalytic Activity of GS-NS@ZIS Core−Shell Particles. Hydrogen production experiments were carried out under irradiation of a 300 W xenon light of intensity 100 mW/cm^2, with the resulting gas collected using a water displacement method. The amount of hydrogen gas collected for the three samples [undoped ZIS, GS-NS(900)@SiO$_2$(17)@ZIS particles, and GS-NS(900)@SiO$_2$(17) particles] is shown in Figure 8a, plotted as a function of time. The hydrogen evolution rate for these samples remained steady for a period of at least 7 h. The rate for the undoped ZIS particles produced an average of 0.05 ± 0.01 L/m^2·h, a value close to that reported in the literature.[23] In addition, the hydrogen production for the GS-NSs without a ZIS shell is negligible. Furthermore, our initial data set showed that all of the ZIS particles containing GS-NSs produced more hydrogen than the undoped ZIS particles, namely, the ZIS particles containing GS-NSs with three different SPR absorptions (~500, 700, and 1000 nm) and three different SiO$_2$ interlayer thicknesses (no SiO$_2$, ~17 nm, and ~42 nm). The data from these experiments are shown Figures S6−S8 in the Supporting Information. To assist in comparisons between samples, we defined a parameter, the "enhancement factor", as the ratio of the average hydrogen evolution rate between the sample of interest and the undoped ZIS sample. The resulting data are shown in Figure 8b.

The data in Figure 8 show that the photocatalytic activity for the ZIS particles containing GS-NSs is noticeably higher than that without GS-NSs. This figure also shows that the samples that incorporate the GS-NSs with the thinner SiO$_2$ interlayer (~17 nm) exhibit the highest photocatalytic activity. However, for the GS-NS-containing particles with no SiO$_2$ interlayer, the activity lies between that of the thin (~17 nm) and thick (~42 nm) SiO$_2$ interlayers. The reduced enhancement compared to the GS-NS(n)@SiO$_2$(17)@ZIS particles can be attributed to the absence of a dielectric interlayer whose blocking ability prevents the photoexcited electrons from transferring back to the GS-NS. Separately, the thicker shell reduces the contribution from the electric field effect upon the surrounding ZIS matrix. Moreover, all of the GS-NSs that have an SPR absorption at 700 nm generated better hydrogen production rates than the samples with SPR absorptions at 500 and 900 nm. Among all of the samples, the GS-NS(700)@SiO$_2$(17)@ZIS particles exhibited the highest enhancement factor (2.6), corresponding to a hydrogen evolution rate of 0.131 ± 0.03 L/m^2·h. Considering these results, an explanation is needed to clarify the role of the interlayer within the GS-NS@ZIS matrix. Therefore, we will discuss charge-transfer mechanisms in the next section.

To understand how the GS-NSs are able to enhance the photocatalytic activity of the ZIS particles, we collected apparent quantum yield data as a function of the wavelength, and we constructed "action spectra" for the hydrogen evolution. Figure 7a plots the extinction spectrum of the undoped ZIS particles and includes the action spectrum (square symbols) for comparison. For the samples that were prepared without nanoshells, the onset of the action spectrum agrees well with that of the extinction spectrum (~550 nm). No hydrogen production was observed in the longer-wavelength region (700−900 nm), and the apparent quantum yield increased with photon energy. It is evident that the ZIS photocatalyst responded to the visible light, and the activity correlates with the band-gap transition between the valence and conduction bands.[3,4] The action spectra of each of the GS-NS(n)@SiO$_2$(17)@ZIS particles (Figure 7b−d) also followed the trends of the individual extinction spectra, indicating an enhancement of hydrogen evolution for the GS-NS-containing ZIS particles at wavelengths from 400 to 700 nm, compared to the pure ZIS photocatalyst. The absorption wavelengths of the SPR bands for the GS-NSs used in this figure were ~500, 700, and 900 nm. For the particles where the SiO$_2$ interlayers were kept at ~17 nm, at the wavelength of 400 nm, the apparent quantum yields of the ZIS particles containing GS-NS(500) and GS-NS(700) are both notably higher than that of the undoped ZIS, with GS-NS(700) producing the largest apparent quantum yield measurement for these data. However, the ZIS containing GS-NS(900) fails to provide a similarly substantial increase. At the longer wavelength of 700 nm, the GS-NS(700)-containing particles again exhibit the highest efficiency. Note that, although the absorption of the GS-NS(900)@SiO$_2$(17)@ZIS particles extends to longer wavelengths, the apparent quantum efficiencies at all wavelengths are smaller than that of the GS-NS(700)@SiO$_2$(17)@ZIS particles, perhaps due a reduction in coupling between the gold nanoshells and the photocatalyst matrix. The apparent quantum yield of the GS-NS(700)@ZIS particles, without the SiO$_2$ interlayer, was also measured and is shown in Figure S9 in the Supporting Information. Once again the action spectrum follows the

extinction spectrum, and the apparent quantum yield is higher than that of the undoped ZIS particles. However, compared to the GS-NS(700)@SiO$_2$(17)@ZIS particles, with the thin SiO$_2$ interlayer, the former exhibits lower apparent quantum yields than the latter. Because of the lower work function of gold, it is likely that the photoexcited electrons, in the absence of the SiO$_2$ interlayer, rapidly transfer back to the gold from the ZIS photocatalyst, leading to a suppressed hydrogen production.

In addition to the quantum efficiency measurements, the luminescence of the core–shell particles can be used to probe the electron–hole recombination probabilities. As demonstrated in the hydrogen evolution rate shown in Figure 8a for the GS-NS@SiO$_2$@ZIS structure, ZIS is the major component that possesses photocatalytic activity. Thus, to investigate the blocking ability of the SiO$_2$ interlayer, we sought to generate photoelectrons within the ZIS and measure the luminescence intensities of samples with different SiO$_2$ thicknesses. Here, GS-NS(700)@SiO$_2$@ZIS particles were used as the model system because absorption of SPR (700 nm) is sufficiently separated from the excitation light source (375 nm), and the GS-NS(700) series exhibited the largest enhancement factors (Figure 8b). In these measurements, we assume that the cocatalyst and SPR effects are decoupled. Figure 9 shows the PL intensities of the
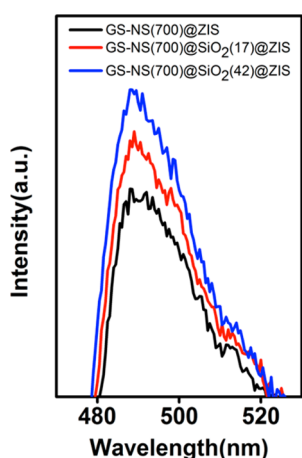

Figure 9. PL intensities for the series of GS-NS(700)@SiO$_2$@ZIS samples upon excitation at 375 nm.

series of GS-NS(700)@SiO$_2$@ZIS particles, where lower PL intensity corresponds to lower recombination probability. The GS-NS(700)@ZIS exhibited the lowest PL, indicating that the GS-NS with no SiO$_2$ coating acts as a sink for the photogenerated electrons. The spectra for the two samples with SiO$_2$ interlayers indicate that the thickest SiO$_2$ interlayer offers the best blocking ability.

Mechanistic Studies. The incorporation of SPR-active metal nanoparticles into semiconductor systems offers a new opportunity to enhance the photocatalytic water splitting, or solar hydrogen production. Most reports utilize small metal nanoparticles (<50 nm) for plasmonic enhancement in photocatalytic reaction studies. However, we used somewhat larger GS-NSs (80 ± 14 nm) for our studies, which might offer an increase in light scattering and an increase of the efficiency. The SPR from metal nanoparticles can facilitate charge separation in the semiconductor through the transfer of plasmonic energy, but it also enhances the complexity of the factors involved in hydrogen evolution.

Although a detailed SPR-mediated charge-separation mechanism remains unclear, a number of mechanisms have been proposed by various research groups.[14] Direct electron transfer (DET) from metal nanoparticles is one means by which enhanced charge and hole generation in the semiconductor has been explained, as has been shown by the plasmonic enhancement for TiO$_2$ systems.[9,12,13] Mubeen et al. reported on their studies of the plasmonic properties for embedded gold nanoparticles in a TiO$_2$ matrix. Their work revealed a dramatic reduction in the dielectric constant for the TiO$_2$ matrix with embedded gold nanoparticles, shifting from 82 (in the dark) to 59 (under visible-light irradiation). These results indicate that the SPR-excited electrons in the gold nanoparticles move into TiO$_2$, thereby reducing the polarizability of the TiO$_2$ matrix as a whole.[35] In these instances, the semiconductor and metal nanoparticles are in direct contact; therefore, hot electrons generated in the metal nanoparticle are able to overcome the Schottky barrier and directly transfer to the semiconductor. Using ejection of the electrons from gold nanoparticles into a sulfide semiconductor as an example; the work function of bulk gold is 5.20 eV, corresponding to 0.7 V vs NHE,[36] and the flat band potential of an n-type metal sulfide semiconductor lies between 0 and −1.0 V vs NHE.[37−40] Assuming an SPR peak absorption of around 700 nm, many of the conduction-band electrons in the gold nanoparticles absorb this photon energy (1.77 eV), but the distribution of energy that occurs because of SPR might lead to individual electrons exceeding the energy associated with the Fermi level (hot electrons). Furube et al. describe a scenario where the plasmon band of the excited electrons in gold overlaps with an interband transition, which would allow filled d-band electrons to be excited to higher electronic states.[9] For our system (see the text above regarding Figure 7),[34] such electrons would be capable of overcoming at least a 1 eV barrier, directly injecting into the semiconductor.[9] However, the probability, or the likelihood, that hot electrons can pass through this barrier is still under investigation.[41−43] White et al. demonstrated that when the photon energy is similar to the barrier height, only a small portion of the electrons can pass through the barrier, but when the photon energy is about twice the barrier height, about 54% of the electrons can pass through the barrier.[44] Therefore, an appropriate matching of the electronic energy levels between the metal particle and the semiconductor enables the DET process to contribute to hydrogen gas evolution. However, the work function of gold is more positive than the conduction-band edge; as a consequence, gold nanoparticles have the capacity to act as cocatalysts and trap photogenerated electrons from the semiconductor.[14] This electron pathway is opposite to that of DET, leading to a competition between DET and the cocatalyst effect.

Two other proposed charge-transfer mechanisms are local electromagnetic field enhancement (LEMF) and resonant energy transfer (RET). The former involves the enhanced electron–hole separation in the semiconductor due to the strong electrical field created in the vicinity of the nanoparticles. This mechanism can facilitate charge separation only for energies above the band gap of the semiconductor.[14] The SPR of metal nanoparticles can also transfer its energy to semiconductor materials through RET, promoting the generation of electron–hole pairs. It is believed that RET is a nonradiative process of the SPR-induced charge-transfer mechanism. Additionally, direct contact between metal nanoparticles and semiconductor is not required, although this near-

field RET effect is restricted by the distance between them.[11,14] To optimize the SPR-mediated energy transfer, the SPR wavelength from the metal nanoparticles must match the energy levels of the semiconductor. In this study, the ability to tune the absorptions of GS-NSs offers an opportunity to optimize the coupling between the SPR of the nanoshells and the band gap of the ZIS photocatalyst. In addition, the optical scattering from our GS-NSs might also contribute to the enhancement of the photocatalytic activity by increasing the path length of light in the ZIS matrix.[11,45]

As shown in Figure 7a, the onset of the absorption of undoped ZIS is ~550 nm, with negligible photocatalytic hydrogen production below the band edge. The apparent quantum yields of the three samples containing GS-NSs coated with a 17 nm SiO_2 shell—GS-NS(500)@SiO_2(17)@ZIS, GS-NS(700)@SiO_2(17)@ZIS, and GS-NS(900)@SiO_2(17)@ZIS—are all higher than that of the undoped ZIS at all wavelengths measured (Figure 7b−d). The higher quantum yields at wavelengths below 550 nm might be attributed to both LEMF and RET. Note also that, at wavelengths above 550 nm (i.e., at energies below the band gap), enhancements at SPR wavelengths were also observed. This increased photocatalytic activity can happen only if the excited plasmonic resonant energy was transferred to the ZIS semiconductor to drive the water reduction for hydrogen evolution. As mentioned in the previous paragraph, for energies below the band gap of ZIS, it is most likely that RET mediates the energy transfer. For our experiments, the absorption of the GS-NSs was systematically varied from 500 to 900 nm; experimental parameters were established with consideration of the overlap between the SPR and ZIS band positions. With these experiments, we found that, independent of the thickness of the SiO_2 interlayer, the GS-NSs with SPR at 700 nm exhibited the highest photocatalytic activity (see Figure 8b). This result suggests that better coupling might exist between the GS-NS(700) core and the surrounding ZIS. In addition, we also observed bending of the ZIS band gap (Figure 7b−d) after incorporating GS-NSs within the ZIS matrix, a phenomenon that might be attributed to the SPR's electric field inducing changes in the photocatalyst.[46] However, the influence upon the photocatalytic activity is still obscure.

In parallel experimental work, we also varied the thickness of the SiO_2 interlayers to provide a means of determining the contributions of the charge-transfer mechanisms, as well as the distance dependence of the RET. A comparison of the composite particles with an ~17 nm SiO_2 interlayer to those with an ~42 nm SiO_2 interlayer shows enhanced hydrogen production for the particles with the thinner interlayer, as shown in Figure 8b. It has been reported in the literature that the range of the intensity of the SPR-generated electromagnetic field is tens of nanometers from the metal core.[14] Our results suggest that the threshold value of the SiO_2 thickness for our particular metal nanostructures lies in the vicinity of ~40 nm (i.e., the limiting distance for the effectiveness of our SPR-generated electromagnetic field). In the case of the samples with no SiO_2 interlayer, the enhancement factors for three GS-NS absorptions are between 1.3 and 1.8, lower than those of the samples with a thinner SiO_2 interlayer (~17 nm) but higher than those with the thicker SiO_2 interlayer (~42 nm). These data indicate that a higher coupling is associated with a shorter distance between the ZIS matrix and the GS-NSs. However, a direct contact between ZIS and the GS-NSs suppresses the electron−hole generation and separation, perhaps because of

the cocatalyst effect (i.e., electron transfer from the semiconductor to the metal nanoparticles). Scheme 1 shows various

Scheme 1. Diagram of the Possible Transfer Mechanisms within the GS-NS@SiO_2@ZIS System
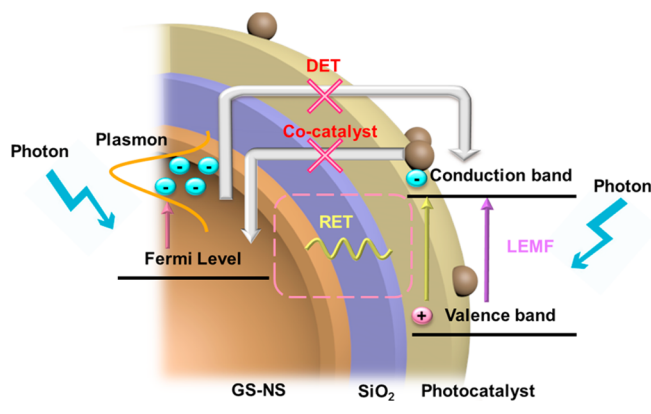
transfer mechanisms that can occur in our GS-NS@SiO_2@ZIS system. The SiO_2 interlayer blocks charge transfer associated with both DET and the cocatalyst effect, whereas LEMF and RET are the two primary charge-transfer mechanisms that can contribute to an enhanced hydrogen production rate at energies above and below the band gap of ZIS, respectively, even with a SiO_2 interlayer present.

CONCLUSIONS

Composite structures based on SiO_2-coated GS-NS cores and ZIS semiconductor shells were fabricated. The photocatalytic activity for hydrogen production from water splitting for these ZIS particles was shown to be adjustable by tuning the SPR absorptions of the GS-NSs in the visible and near-IR region and by introducing and modulating the thickness of the SiO_2 interlayer between the embedded GS-NSs and the ZIS matrix. The GS-NS(700)@SiO_2(17)@ZIS particles exhibited the highest hydrogen production rate of 0.131 ± 0.03 L/m^2·h, an amount that represented an enhancement of 2.6 times the rate of the ZIS matrix alone. The presence of GS-NSs in the ZIS matrix extended the absorption/scattering of the system to longer wavelengths and increased the apparent quantum yields to energies lower than the band gap of ZIS. Our experimental findings demonstrate that (1) the coupling between the SPR of the GS-NSs and the absorption of the ZIS photocatalyst and (2) the presence and thickness of the SiO_2 interlayer separating these two materials are two key parameters necessary to optimize solar hydrogen production. As a consequence, this study provides important information for the design of the next generation of composite materials for hydrogen production from water splitting.

ASSOCIATED CONTENT

Ⓢ Supporting Information

The Supporting Information is available free of charge on the ACS Publications website at DOI: 10.1021/acsami.6b01197.

> SEM images of silver nanoparticles and GS-NSs, particle size distribution histograms, EDX elemental mapping data, a TEM image that verifies the stability of the SiO_2 shell under harsh acidic conditions, plots of hydrogen evolution, and a UV−vis spectrum with apparent

quantum yield data for the GS-NS(700)@ZIS particles (Figures S1−S9) (PDF)

■ AUTHOR INFORMATION

Corresponding Authors
*E-mail: trlee@uh.edu.
*E-mail: taichoulee@ncu.edu.tw.

Author Contributions
§These individuals contributed equally to this effort.

Notes
The authors declare no competing financial interest.

■ ACKNOWLEDGMENTS

■ REFERENCES

(1) Zweibel, K.; Mason, J.; Fthenakis, V. A Solar Grand Plan. *Sci. Am.* **2008**, *298*, 64−73.

(2) Roy, S. C.; Varghese, O. K.; Paulose, M.; Grimes, C. A. Toward Solar Fuels: Photocatalytic Conversion of Carbon Dioxide to Hydrocarbons. *ACS Nano* **2010**, *4*, 1259−1278.

(3) Kudo, A.; Miseki, Y. Heterogeneous Photocatalyst Materials for Water Splitting. *Chem. Soc. Rev.* **2009**, *38*, 253−278.

(4) Kudo, A. Recent Progress in the Development of Visible Light-Driven Powdered Photocatalysts for Water Splitting. *Int. J. Hydrogen Energy* **2007**, *32*, 2673−2678.

(5) Li, Z.; Luo, W.; Zhang, M.; Feng, J.; Zou, Z. Photo-electrochemical Cells for Solar Hydrogen Production: Current State of Promising Photoelectrodes, Methods to Improve Their Properties, and Outlook. *Energy Environ. Sci.* **2013**, *6*, 347−370.

(6) Chen, X.; Shen, S.; Guo, L.; Mao, S. S. Semiconductor-Based Photocatalytic Hydrogen Generation. *Chem. Rev.* **2010**, *110*, 6503−6570.

(7) Gust, D.; Moore, T. A.; Moore, A. L. Solar Fuels via Artificial Photosynthesis. *Acc. Chem. Res.* **2009**, *42*, 1890−1898.

(8) Tong, H.; Ouyang, S.; Bi, Y.; Umezawa, N.; Oshikiri, M.; Ye, J. Nano-Photocatalytic Materials: Possibilities and Challenges. *Adv. Mater.* **2012**, *24*, 229−251.

(9) Furube, A.; Du, L.; Hara, K.; Katoh, R.; Tachiya, M. Ultrafast Plasmon-Induced Electron Transfer from Gold Nanodots into TiO_2 Nanoparticles. *J. Am. Chem. Soc.* **2007**, *129*, 14852−14853.

(10) Jiang, D.; Zhou, W.; Zhong, X.; Zhang, Y.; Li, X. Distinguishing Localized Surface Plasmon Resonance and Schottky Junction of Au−Cu_2O Composites by Their Molecular Spacer Dependence. *ACS Appl. Mater. Interfaces* **2014**, *6*, 10958−10962.

(11) Zhou, J.; Ren, F.; Zhang, S.; Wu, W.; Xiao, X.; Liu, Y.; Jiang, C. SiO_2-Ag-SiO_2-TiO_2 Multi-Shell Structures: Plasmon Enhanced Photocatalysts with Wide-Spectral-Response. *J. Mater. Chem. A* **2013**, *1*, 13128−13138.

(12) Zhang, Z.; Wang, Z.; Cao, S.-W.; Xue, C. Au/Pt Nanoparticle-Decorated TiO_2 Nanofibers with Plasmon-Enhanced Photocatalytic Activities for Solar-to-Fuel Conversion. *J. Phys. Chem. C* **2013**, *117*, 25939−25947.

(13) Kochuveedu, S. T.; Kim, D.-P.; Kim, D. H. Surface-Plasmon-Induced Visible Light Photocatalytic Activity of TiO_2 Nanospheres Decorated by Au Nanoparticles with Controlled Configuration. *J. Phys. Chem. C* **2012**, *116*, 2500−2506.

(14) Cushing, S. K.; Li, J.; Meng, F.; Senty, T. R.; Suri, S.; Zhi, M.; Li, M.; Bristow, A. D.; Wu, N. Photocatalytic Activity Enhanced by Plasmonic Resonant Energy Transfer from Metal to Semiconductor. *J. Am. Chem. Soc.* **2012**, *134*, 15033−15041.

(15) Li, J.; Cushing, S. K.; Bright, J.; Meng, F.; Senty, T. R.; Zheng, P.; Bristow, A. D.; Wu, N. Ag@Cu_2O Core-Shell Nanoparticles as Visible-Light Plasmonic Photocatalysts. *ACS Catal.* **2013**, *3*, 47−51.

(16) Chen, J.-J.; Wu, J. C. S.; Wu, P. C.; Tsai, D. P. Plasmonic Photocatalyst for H_2 Evolution in Photocatalytic Water Splitting. *J. Phys. Chem. C* **2011**, *115*, 210−216.

(17) Takahashi, T.; Kudo, A.; Kuwabata, S.; Ishikawa, A.; Ishihara, H.; Tsuboi, Y.; Torimoto, T. Plasmon-Enhanced Photoluminescence and Photocatalytic Activities of Visible-Light-Responsive ZnS-$AgInS_2$ Solid Solution Nanoparticles. *J. Phys. Chem. C* **2013**, *117*, 2511−2520.

(18) Agnihotri, S.; Mukherji, S.; Mukherji, S. Size-Controlled Silver Nanoparticles Synthesized Over the Range 5−100 nm Using the Same Protocol and Their Antibacterial Efficacy. *RSC Adv.* **2014**, *4*, 3974−3984.

(19) Ziegler, C.; Eychmüller, A. Seeded Growth Synthesis of Uniform Gold Nanoparticles with Diameters of 15−300 nm. *J. Phys. Chem. C* **2011**, *115*, 4502−4506.

(20) Shen, J.; Zai, J.; Yuan, Y.; Qian, X. 3D Hierarchical $ZnIn_2S_4$: The Preparation and Photocatalytic Properties on Water Splitting. *Int. J. Hydrogen Energy* **2012**, *37*, 16986−16993.

(21) Wang, T. X.; Xu, S. H.; Yang, F. X. $ZnIn_2S_4$ Nanopowder as An Efficient Visible Light-Driven Photocatalyst in the Reduction of Aqueous Cr(VI). *Mater. Lett.* **2012**, *83*, 46−48.

(22) Shen, S.; Chen, J.; Wang, X.; Zhao, L.; Guo, L. Microwave-Assisted Hydrothermal Synthesis of Transition-Metal Doped $ZnIn_2S_4$ and Its Photocatalytic Activity for Hydrogen Evolution Under Visible Light. *J. Power Sources* **2011**, *196*, 10112−10119.

(23) Shen, S.; Zhao, L.; Guo, L. Cetyltrimethylammoniumbromide (CTAB)-Assisted Hydrothermal Synthesis of $ZnIn_2S_4$ as An Efficient Visible-Light-Driven Photocatalyst for Hydrogen Production. *Int. J. Hydrogen Energy* **2008**, *33*, 4501−4510.

(24) Vongsavat, V.; Vittur, B. M.; Bryan, W. W.; Kim, J.-H.; Lee, T. R. Ultrasmall Hollow Gold−Silver Nanoshells with Extinctions Strongly Red-Shifted to the Near-Infrared. *ACS Appl. Mater. Interfaces* **2011**, *3*, 3616−3624.

(25) Yang, Y.; Shi, J.; Kawamura, G.; Nogami, M. Preparation of Au−Ag, Ag−Au Core−Shell Bimetallic Nanoparticles for Surface-Enhanced Raman Scattering. *Scr. Mater.* **2008**, *58*, 862−865.

(26) Lee, P. C.; Meisel, D. Adsorption and Surface-Enhanced Raman of Dyes on Silver and Gold Sols. *J. Phys. Chem.* **1982**, *86*, 3391−3395.

(27) Oldenburg, S. J.; Averitt, R. D.; Westcott, S. L.; Halas, N. J. Nanoengineering of Optical Resonances. *Chem. Phys. Lett.* **1998**, *288*, 243−247.

(28) Stober, W.; Fink, A.; Bohn, E. Controlled Growth of Monodisperse Silica Spheres in the Micron Size Range. *J. Colloid Interface Sci.* **1968**, *26*, 62−69.

(29) Wu, C.-C.; Cho, H.-F.; Chang, W.-S.; Lee, T.-C. A Simple and Environmentally Friendly Method of Preparing Sulfide Photocatalyst. *Chem. Eng. Sci.* **2010**, *65*, 141−147.

(30) Li, C.-H.; Jamison, A. C.; Rittikulsittichai, S.; Lee, T.-C.; Lee, T. R. In situ Growth of Hollow Gold-Silver Nanoshells within Porous Silica Offers Tunable Plasmonic Extinctions and Enhanced Colloidal Stability. *ACS Appl. Mater. Interfaces* **2014**, *6*, 19943−19950.

(31) Hao, E.; Li, S.; Bailey, R. C.; Zou, S.; Schatz, G. C.; Hupp, J. T. Optical Properties of Metal Nanoshells. *J. Phys. Chem. B* **2004**, *108*, 1224−1229.

(32) Philipse, A. P.; Vrij, A. Preparation and Properties of Nonaqueous Model Dispersions of Chemically Modified, Charged Silica Spheres. *J. Colloid Interface Sci.* **1989**, *128*, 121−136.

(33) Li, E. Q.; Vakarelski, I. U.; Chan, D. Y. C.; Thoroddsen, S. T. Stabilization of Thin Liquid Films by Repulsive van der Waals Force. *Langmuir* **2014**, *30*, 5162−5169.

(34) Wu, D.; Liu, X. Optimization of the Bimetallic Gold and Silver Alloy Nanoshell for Biomedical Applications In Vivo. *Appl. Phys. Lett.* **2010**, *97*, 061904.

(35) Mubeen, S.; Hernandez-Sosa, G.; Moses, D.; Lee, J.; Moskovits, M. Plasmonic Photosensitization of a Wide Band Gap Semiconductor:

Converting Plasmons to Charge Carriers. *Nano Lett.* **2011**, *11*, 5548−5552.

(36) Khoa, N. T.; Kim, S. W.; Yoo, D.-H.; Kim, E. J.; Hahn, S. H. Size-Dependent Work Function and Catalytic Performance of Gold Nanoparticles Decorated Graphene Oxide Sheets. *Appl. Catal., A* **2014**, *469*, 159−164.

(37) Cheng, K.-W.; Lee, W.-C.; Fan, M.-S. Photoelectrochemical Performance of Cu−Zn−In−S Film Grown Using One-Step Electrodeposition. *Electrochim. Acta* **2013**, *87*, 53−62.

(38) Wang, C.-H.; Cheng, K.-W.; Tseng, C.-J. Photoelectrochemical Properties of AgInS$_2$ Thin Films Prepared Using Electrodeposition. *Sol. Energy Mater. Sol. Cells* **2011**, *95*, 453−461.

(39) Lee, F.-Y.; Yang, K.-Y.; Wang, Y.-C.; Li, C.-H.; Lee, T. R.; Lee, T.-C. Electrochemical Properties of an AgInS$_2$ Photoanode Prepared Using Ultrasonic-Assisted Chemical Bath Deposition. *RSC Adv.* **2014**, *4*, 35215−35223.

(40) Chang, W.-S.; Wu, C.-C.; Jeng, M.-S.; Cheng, K.-W.; Huang, C.-M.; Lee, T.-C. Ternary Ag-In-S Polycrystalline Films Deposited Using Chemical Bath Deposition for Photoelectrochemical Applications. *Mater. Chem. Phys.* **2010**, *120*, 307−312.

(41) Manjavacas, A.; Liu, J. G.; Kulkarni, V.; Nordlander, P. Plasmon-Induced Hot Carriers in Metallic Nanoparticles. *ACS Nano* **2014**, *8*, 7630−7638.

(42) Sundararaman, R.; Narang, P.; Jermyn, A. S.; Goddard III, W. A.; Atwater, H. A. Theoretical Predictions for Hot-Carrier Generation from Surface Plasmon Decay. *Nat. Commun.* **2014**, *5*, 5788.

(43) Marchuk, K.; Willets, K. A. Localized Surface Plasmons and Hot Electrons. *Chem. Phys.* **2014**, *445*, 95−104.

(44) White, T. P.; Catchpole, K. R. Plasmon-Enhanced Internal Photoemission for Photovoltaics: Theoretical Efficiency Limits. *Appl. Phys. Lett.* **2012**, *101*, 073905.

(45) Kumar, M. K.; Krishnamoorthy, S.; Tan, L. K.; Chiam, S. Y.; Tripathy, S.; Gao, H. Field Effects in Plasmonic Photocatalyst by Precise SiO$_2$ Thickness Control Using Atomic Layer Deposition. *ACS Catal.* **2011**, *1*, 300−308.

(46) Zhang, Z.; Yates, J. T., Jr. Band Bending in Semiconductors: Chemical and Physical Consequences at Surfaces and Interfaces. *Chem. Rev.* **2012**, *112*, 5520−5551.